Invited extended paper from Eighth International Conference on Numerical Methods in Laminar and Turbulent Flow, which was held July 1993 at Swansea, U.K. The guest editor is Prof. Samuel H. Makarios of Ain Shams University, Cairo, Egypt.

NAVIER–STOKES COMPUTATIONS OF HYPERSONIC FLOWS

R. HILLIER, D. KIRK AND S. SOLTANI

Department of Aeronautics, Imperial College of Science, Technology and Medicine, London SW7 2BY, U.K.

ABSTRACT

The current interest in hypersonic flows is leading to significant effort both to develop CFD methods and also to provide experimental data for their evaluation. In our research we attempt to integrate CFD and experiments as closely as possible so much so that most of our experimental model designs are based upon preliminary flow field computations in order to identify likely regions of importance and distribute instrumentation as efficiently as possible. The experiments must also have the CFD requirements clearly in mind. In particular we consider it important to separate evaluation on the *numerics* (essentially the algorithm) from modelling of the *physics* (which includes the uncertainties of turbulence modelling); to this end our experiments include laminar studies, for both attached and separated flows, for which the physical equations are known exactly, as well as turbulent flow studies. This paper concentrates mainly on our CFD efforts and presents details of a high resolution solver for viscous flows together with their predictions for a range of problems which are the subject of our current and planned experiments.

KEY WORDS   Hypersonic flows   Navier–Stokes equations

THE FLOW SOLVER

In cylindrical coordinates the two-dimensional Navier Stokes equations are:

$$\frac{\partial U}{\partial t}+\frac{\partial E_H}{\partial x}+\frac{\partial F_H}{\partial y}+\frac{(F_H+G_H)}{y}=\frac{\partial E_v}{\partial x}+\frac{\partial F_v}{\partial y}+\frac{(F_v+G_v)}{y} \tag{1}$$

Here y is the radial distance from the axis of symmetry and the vectors U, E, F and G are given by:

$$U=\begin{vmatrix} \rho \\ \rho u \\ \rho v \\ \rho e \end{vmatrix} \quad E_H=\begin{vmatrix} \rho u \\ p+\rho u^2 \\ \rho uv \\ u(p+\rho e) \end{vmatrix} \quad F_H=\begin{vmatrix} \rho v \\ \rho uv \\ p+\rho v^2 \\ v(p+\rho e) \end{vmatrix} \quad G_H=\begin{vmatrix} 0 \\ 0 \\ -p \\ 0 \end{vmatrix} \tag{2}$$

$$E_v=\begin{vmatrix} 0 \\ \tau_{xx} \\ \tau_{xy} \\ -q_{xx}+u\tau_{xx}+v\tau_{xy} \end{vmatrix} \quad F_v=\begin{vmatrix} 0 \\ \tau_{xy} \\ \tau_{yy} \\ -q_{yy}+u\tau_{xy}+v\tau_{yy} \end{vmatrix} \quad G_v=\begin{vmatrix} 0 \\ 0 \\ -\tau_{\theta\theta} \\ 0 \end{vmatrix} \tag{3}$$

where subscripts H and v refer to the hyperbolic and diffusive viscous terms respectively. For

a laminar flow the viscous terms are given by:

$$\tau_{xx} = (\lambda + 2\mu)\frac{\partial u}{\partial x} + \frac{\lambda}{y}\frac{\partial}{\partial y}(yv), \qquad \tau_{xy} = \mu\left(\frac{\partial u}{\partial y} + \frac{\partial v}{\partial x}\right)$$

$$\tau_{yy} = (\lambda + 2\mu)\frac{\partial v}{\partial y} + \lambda\left(\frac{\partial u}{\partial x} + \frac{v}{y}\right), \qquad \tau_{\theta\theta} = (\lambda + 2\mu)\frac{v}{y} + \lambda\left(\frac{\partial u}{\partial x} + \frac{\partial v}{\partial y}\right)$$

$$q_{xx} = -k\frac{\partial T}{\partial x}, \qquad q_{yy} = -k\frac{\partial T}{\partial y}, \qquad k = \frac{c_p\mu}{Pr}, \qquad \lambda = -\frac{2}{3}\mu \tag{4}$$

Our solution procedure for (1) is to employ 'convection-diffusion splitting' whereby the solution is advanced one time step by separate evaluations of the convective and diffusive terms.

For the inviscid solver we have used an explicit second order upwind Godunov-type scheme, extended from the work of Ben-Artzi and Falcotivz[1,2], which provides high resolution capture of pressure waves and vortical structures. The basic feature of this calculation is that using the initial cell-average values piecewise linear second order spatial gradients are specified for the flow variables. At cell interfaces this provides discontinuities in flow variables and their gradients. Solution of this generalised Riemann problem (GRP) at the interface then provides a second order accurate flux. No explicit artificial viscosity is used; however in the initial specification of the cell gradients a monotone constraint is applied to prevent the formation of new extrema. We have developed this approach for two-dimensional problems using both operator splitting and an unsplit solver[3-5]. Here we have used the split solver since it is more suitable for the high aspect ratio cells associated with a Navier–Stokes calculation.

The viscous step, that is the solution of:

$$\frac{\partial \mathbf{U}}{\partial t} = \frac{\partial \mathbf{E}_v}{\partial x} + \frac{\partial \mathbf{F}_v}{\partial y} + \frac{(\mathbf{F}_v + \mathbf{G}_v)}{y} \tag{5}$$

uses a centred difference solver. This is relatively simple since the density remains constant (in the mass equation $\mathbf{E}_v$, $\mathbf{F}_v$ and $\mathbf{G}_v$ all equal zero) and the momentum equations can be uncoupled from the energy equation. The solution can then readily be accomplished with either explicit or implicit formulations.

Coupling of the viscous and inviscid solvers uses a symmetric operator, for example:

$$\mathbf{U}^{n+1} = \mathbf{L}_v\left(\frac{\Delta t}{2}\right)\mathbf{L}_H(\Delta t)\mathbf{L}_v\left(\frac{\Delta t}{2}\right)\mathbf{U}^n \tag{6}$$

The calculation of surface heat transfer rates uses the laminar formulation $q_{wall} = -k\left.\frac{\partial T}{\partial n}\right|_{wall}$,

where $\frac{\partial T}{\partial n}$ is the wall-normal temperature gradient. For the turbulent boundary layer calculations the first cell from the wall has a y^+ value of less than 1.0, ensuring both the correctness of usage of a laminar formulation and precision in the estimation of the temperature gradient. Many of our calculations have involved hypersonic attached boundary layers. For these we have developed a 'block marching' procedure, coupled with the thin layer form of the Navier–Stokes equations. In this we achieve some of the advantages of a parabolised Navier–Stokes method. The computation is confined to a restricted domain block as shown in *Figure 1*, generally of 10 to 15 cells extent in the flow direction; once the upstream columns of the block are converged the block is shifted one cell in the flow direction and the procedure is continued. This produces an efficient solution, partly because the upstream zones of the flow field must physically reach steady state before regions further downstream and it is wasteful to iterate them unnecessarily and partly because the calculation can also proceed at the optimum time step for the block rather than being constrained by the whole flow field. The second feature that we have introduced
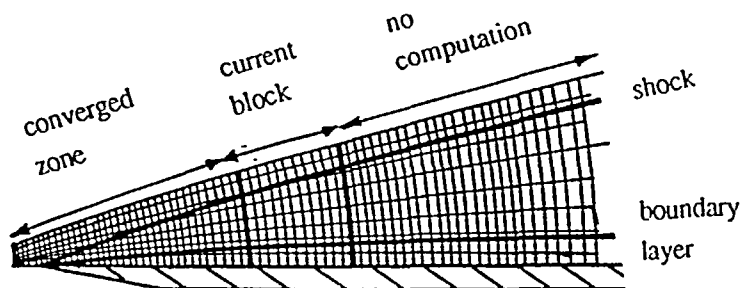
Figure 1 Schematic of mesh for the block marching calculation. With the adaptive mesh construction the streamwise mesh surfaces are distorted so that they align with the shock wave or boundary layer edge as appropriate

is a mesh construction technique, coupled with the block marching, which seeks to optimise the mesh within the constraints of a structured arrangement. Its implementation is illustrated in the schematic of *Figure 1*. We essentially declare the number of cells required from the body to the boundary layer edge, and from the body to the leading edge shock, so that the solution is computed to the same level of resolution at all chordwise stations. At present we start the calculation with a fixed block at the leading edge, so that the solution only converges on to the required mesh refinement some distance downstream. It is clearly easy to extend this logic, for example by setting the number of cells from the wall to the temperature maximum in the boundary layer (which is an important control on the accuracy of heat transfer modelling) or by employing adaptive control over the critical inner wall scales of a turbulent boundary layer.

SOLUTION OF THE FLAT PLATE BOUNDARY LAYER

We have performed a range of evaluation calculations for the code, both inviscid and laminar viscous, including flat plates, sharp and blunted cones and wedge flows, Reference 6. For demonstration here the solution is shown for the flat plate laminar boundary layer, which can be compared with the theoretical predictions by Van Driest[7]. We have chosen the case of Mach 8.0, with a wall/free stream temperature ratio of 6.0, since these are close to the experimental conditions in our hypersonic wind tunnel. We use a mesh with 117 cells along the suface of the plate up to a chord Reynolds number of 3.8 million. A chordwise stretching factor of 1.025 is used for these cells giving a cell Reynolds number $\left(\dfrac{\rho_\infty U_\infty \Delta x}{\mu_\infty} \right)$ of 5600 at the leading edge and 99 000 at the trailing edge. Three computations are performed, one with 10 cells from the body to the boundary layer edge and a further 10 to the shock (which arises from the leading edge viscous interaction) then a doubling and further doubling of these numbers. Physically, this flow is characterised by a marked viscous interaction, the displacement effect of the boundary layer on the external flow producing elevated pressures on the surface. *Figure 2* shows this surface pressure variation, with chordwise Reynolds number, whilst *Figure 3* shows the cross plane density contours, identifying both the bundary layer and the viscously driven leading edge shock. *Figures 4, 5* and *6* present profiles of density, Mach number and *u*-component of velocity, in each case normalised by their free stream values, at a station with a chordwise Reynolds number of three million. The three levels of mesh refinement show excellent agreement with each other both for the boundary layer and also for the external inviscid flow. The Van Driest calculations are for genuinely zero pressure gradient, whereas we have seen that the computations experience a pressure gradient due to the leading edge interaction, so that comparison with Van Driest is therefore not exactly like for like. The velocity profile will be the best basis for comparison since at hypersonic speeds it is least responsive to pressure gradients and *Figure 6* shows excellent
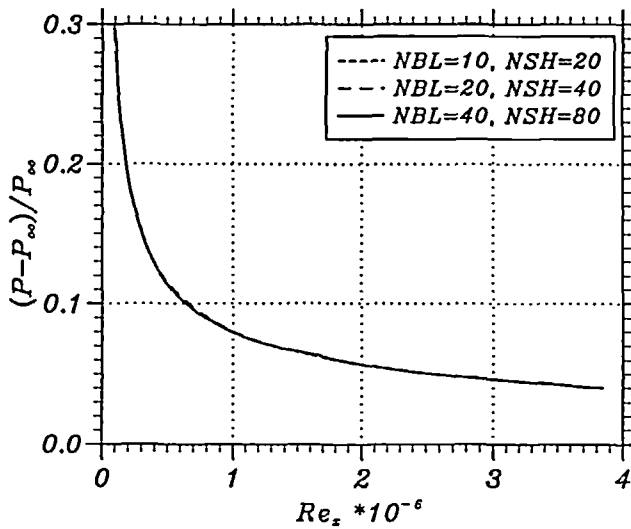
Figure 2   Laminar flat plate boundary layer computation with $M_x = 8.0$, $T_w/T_x = 6.0$. Variation of induced pressure, due to the viscous interaction, with chord Reynolds number. NBL and NSH show the number of mesh points from the body to the boundary layer and shock respectively
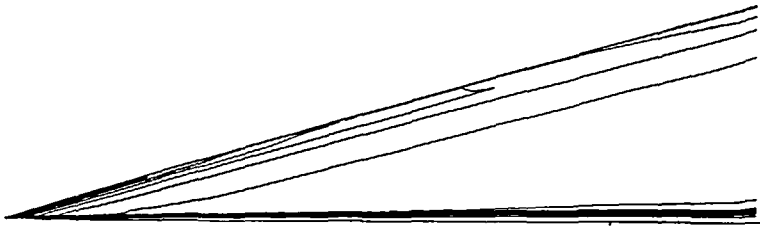

Figure 3   Density contours showing the boundary layer and the viscous interaction induced leading edge shock. The vertical axis is stretched by a factor of 2.0

agreement between CFD and theory. The comparison in *Figure 7* presents surface heat transfer rates $\dot{q}_w$ as Stanton number, defined as

$$St = \frac{\dot{q}_w}{\rho_\infty U_\infty c_p (T_r - T_w)} \tag{7}$$

versus chordwise Reynolds number. Again, very close agreement with the theoretical solution is found.

LAMINAR HYPERSONIC ATTACHED AND SEPARATED SHEAR LAYER COMPUTATIONS

Having shown the accuracy of the scheme for computation of laminar flow over a flat plate, it has then been used in the aerodynamic design of a model for an experimental study of hypersonic laminar separated flows. These experiments, in turn, will define a set of data for CFD evaluation
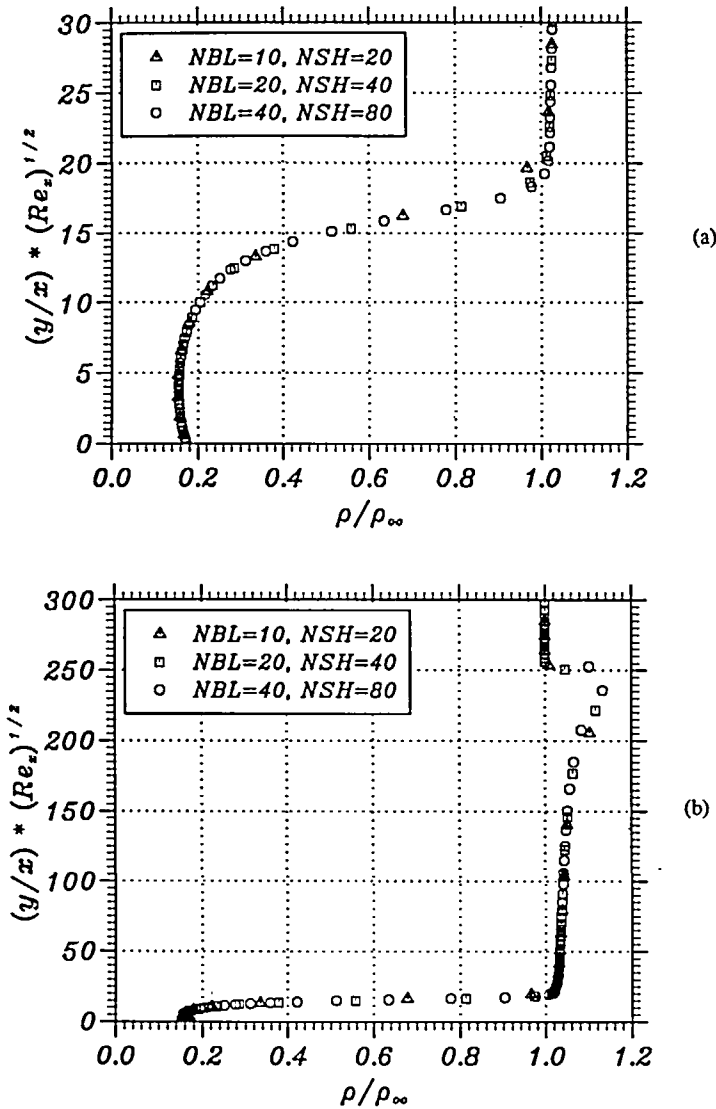
Figure 4 Density profile presented at a chord Reynolds number of 3 million for three levels of mesh refinement. The boundary layer edge and shock wave are at scaled thickneses of 25 and 250 respectively. (a) shows the boundary layer detail and (b) the detail through the whole shock layer

and validation. The experiments are being conducted in the Imperial College gun tunnel where the nominal low Reynolds number test section conditions using nitrogen gas are $M_\infty = 8.1$, $Re_\infty = 6.5 \times 10^6/\text{m}$; $T_o = 1050$ K. A cavity is selected as the basic separation configuration resulting in a fixed separation point and an essentially known reattachment point. The model must satisfy these requirements:

- The model must be axisymmetric. This is to avoid the three-dimensional end effects which would be generated by a planar 2-D model. A secondary reason is that the tunnel test section experiences mild axial flow gradients, whilst maintaining axisymmetry, so that an axisymmetric configuration will again preserve a better quality of two-dimensionality.
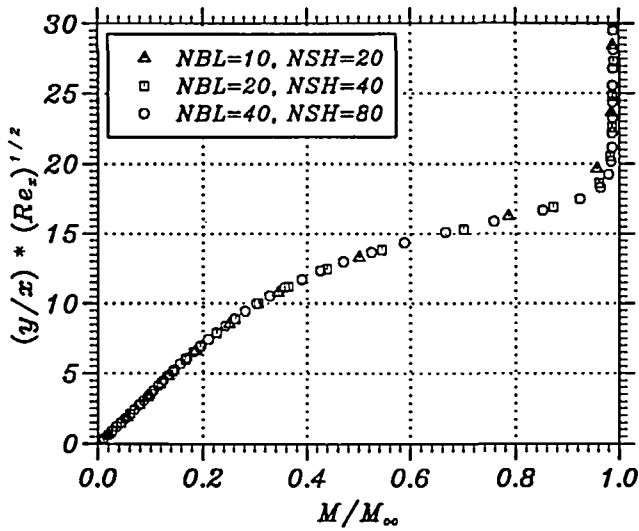
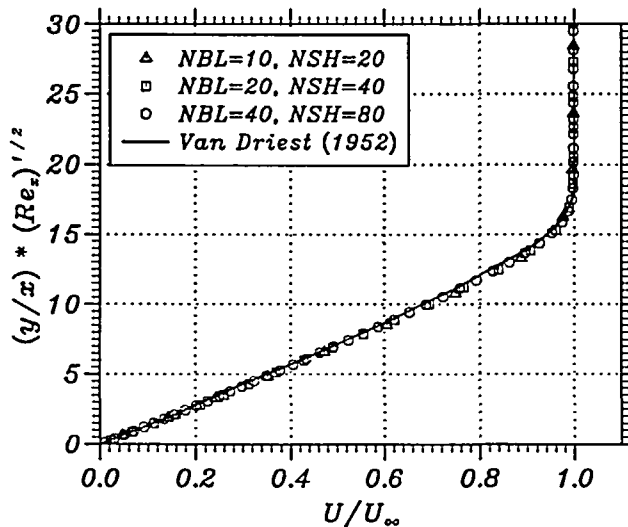*Figure 5*   Mach number profile. Legend as for *Figure 4*

Figure 6   Velocity profile. legend as for *Figure 4*. The theoretical zero pressure gradient solution of Van Driest is included

- The model consists of a forebody which generates an attached boundary layer and a variable geometry cavity which provides the separated flow field.
- The approaching boundary layer must be laminar and should remain so after separation and subsequent reattachment.
- The boundary layer at separation should be of measurable thickness ($\delta_{99\%} > 2$ mm) and the streamwise variation of the edge conditions should be as small as possible.
- In order to have good spatial resolution, cavity depth must be as large as possible. It is also desirable to have a small ratio of cavity depth to radial distance from the axis of symmetry.
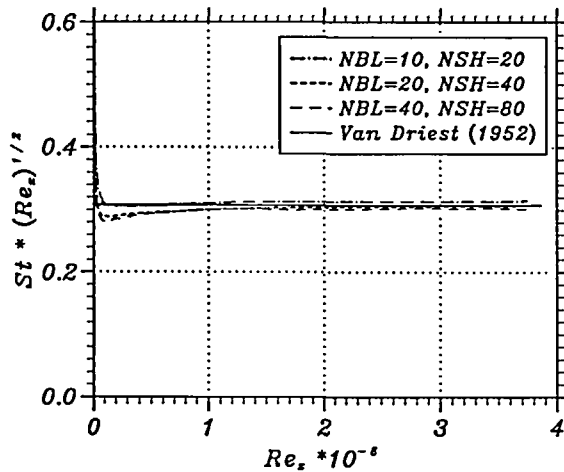
Figure 7 Surface heating presented as Stanton number. The theoretical Van Driest solution takes no account of the leading edge viscous interaction
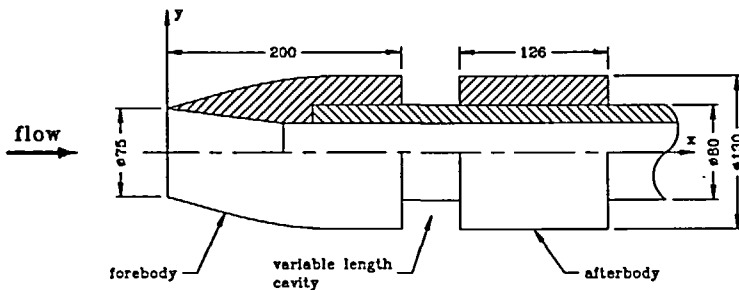

Figure 8 Schematic of the forebody/cavity-separation model

Based on the above requirements, the proposed configuration is a hollow cylindrical model as shown in *Figure 8*. The forebody shape has been arrived at by computing the flow field around provisional configurations until the design requirements are met. The forebody coordinates are detailed in Appendix 1.

The first computations presented are for the forebody alone and have been performed using the TSL option of the code, with adaptive mesh movement, including the appropriate axisymmetric terms. A constant model surface temperature of 295 K has been used throughout. Three grids have been used in order to assess the mesh independence of the solution. The first grid has 10 cells in the boundary layer and 20 cells from the body to the shock wave (NBL = 10, NSH = 20). The corresponding numbers for the second and the third grid are NBL = 20, NSH = 40 and NBL = 40, NSH = 80, so that the solution quality should be of the same order as that shown in the previous section for the flat plate. In the experiments the separation will be fixed at $x = 200$ mm, but the first forebody here is extended to $x = 400$ mm in order to assess the likely edge conditions for the cavity flow. *Figure 9* shows the surface pressure distributions for the three meshes, using 230 cells over the 400 mm chord with the three curves so close as to be indistinguishable. The pressure varies continuously and smoothly from the leading edge to the 'separation point'. Moreover, the surface pressure after $x = 200$ mm is virtually constant so that
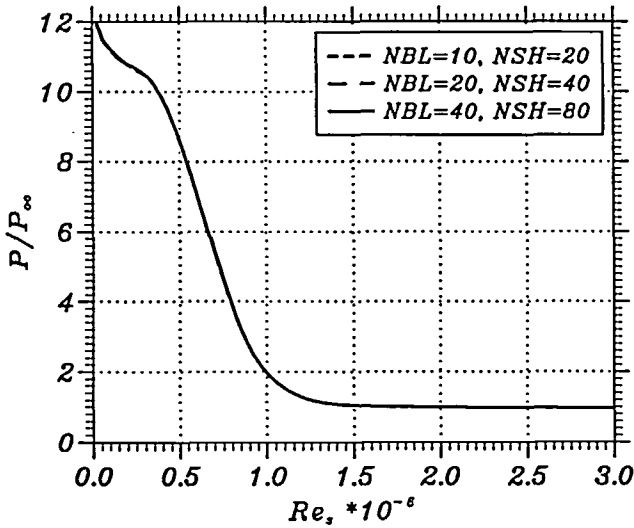
Figure 9 Computed surface pressure distribution for forebody extending to 400 mm with no cavity and with three levels of mesh refinement
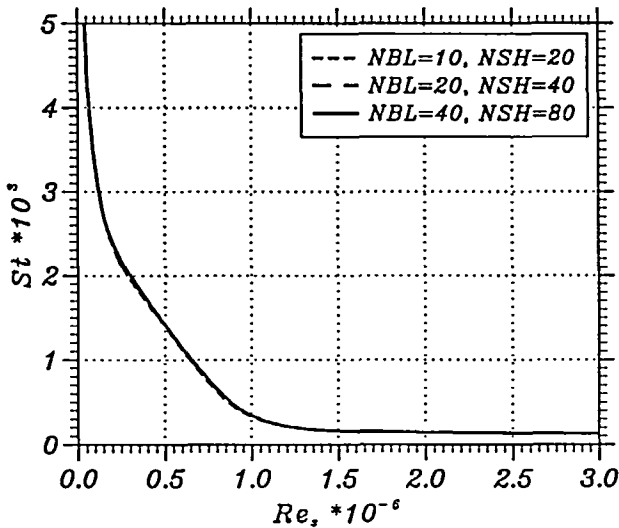

Figure 10 Stanton number distribution on forebody

any cavity located here would not experience pressure gradients generated by the forebody. Distributions of the Stanton number are shown in *Figure 10*, again the three curves being virtually indistinguishable. Boundary layer profiles of velocity, temperature and Mach number at the 'separation point' (i.e. at $x = 200$ mm) are compared in *Figures 11, 12* and *13* respectively. These results show an excellent agreement between the solutions obtained on the three grids. The boundary layer thickness from *Figure 11* is about 4 mm which is large enough for accurate measurement.
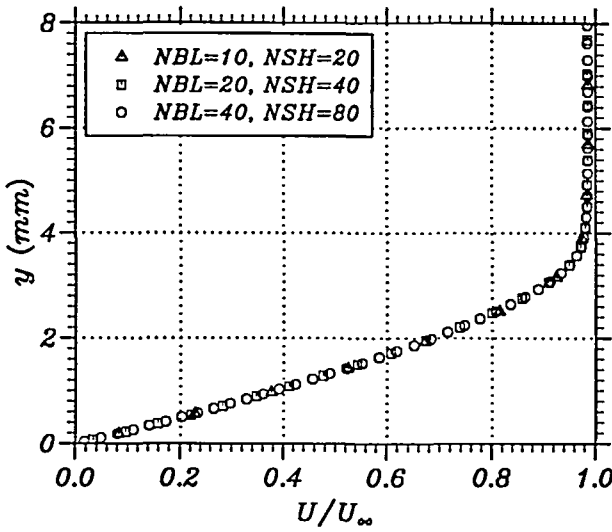
Figure 11 Boundary layer velocity profile, on forebody, at the proposed cavity leading edge position ($x = 200$ mm)
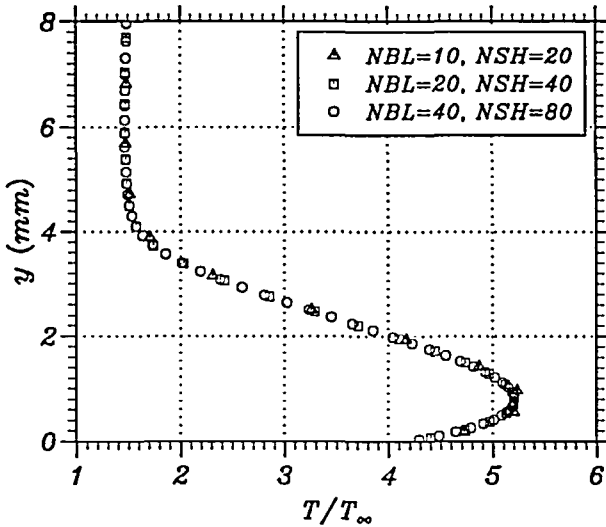

Figure 12 Computed temperature profile

The cavity flow is next calculated by the full Navier–Stokes option of the code. Here the results for a cavity with a length to depth ratio of unity, cavity length Reynolds number $Re_L = 162500$, are presented. The computational field starts from 15 mm upstream of the separation point, using the previous forebody solution as initial conditions, and extends for 50 mm downstream of reattachment. Three grids have been used in order to assess the mesh dependency of the solution. The upper part of the grid, for all three meshes, is generated using the adapted mesh from the previous forebody computations with NBL = 20 and NSH = 40. The
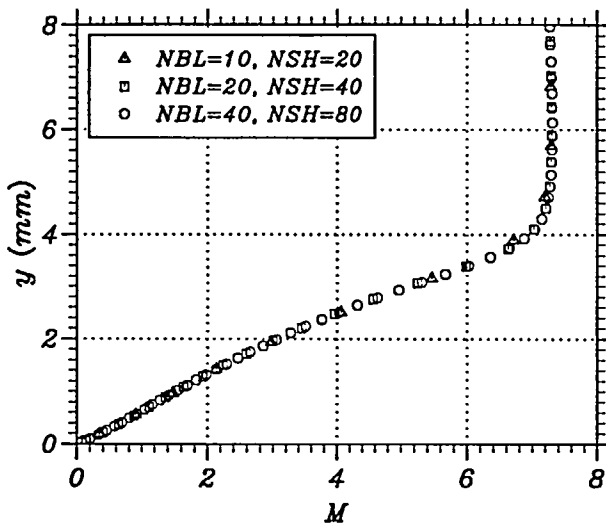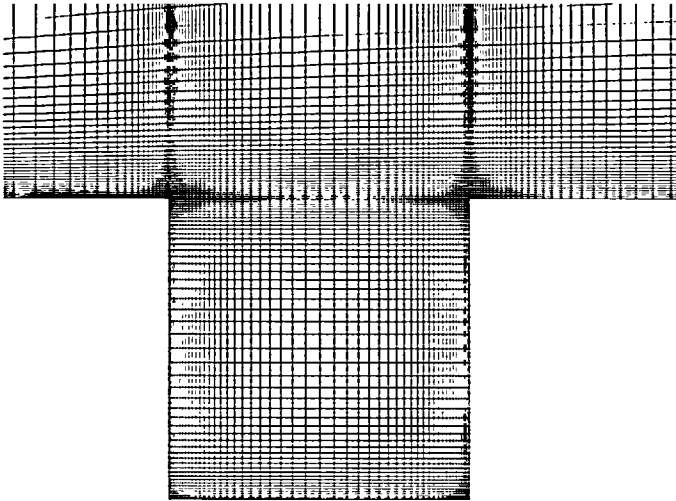
Figure 13 Computed Mach number profile

Figure 14 Mesh for laminar cavity computation. Length (L) and depth (D) are both 25 mm. Reynolds number based on cavity length is 162500

mesh within the cavity is rectangular with appropriate stretching so that a smooth variation of cell size, in both I and J directions, is maintained. There are 30 cells in each direction within the cavity for the first mesh. This number is increased to 40 and 50 for the second and the third mesh respectively. Part of the finest mesh (50 by 50 cells in the cavity) is shown in *Figure 14*. *Figure 15* presents the velocity vectors within the cavity for this case, indicating a main vortex and two secondary vortices near the bottom corners. Variation of surface pressure with X/D for the three meshes is presented in *Figure 16*. Here X is the 'wetted' distance from the separation
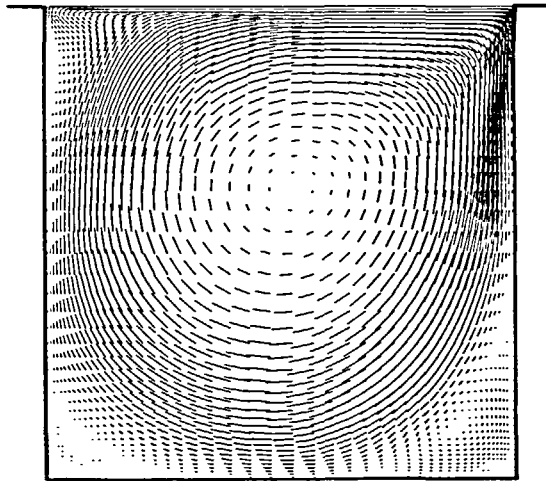
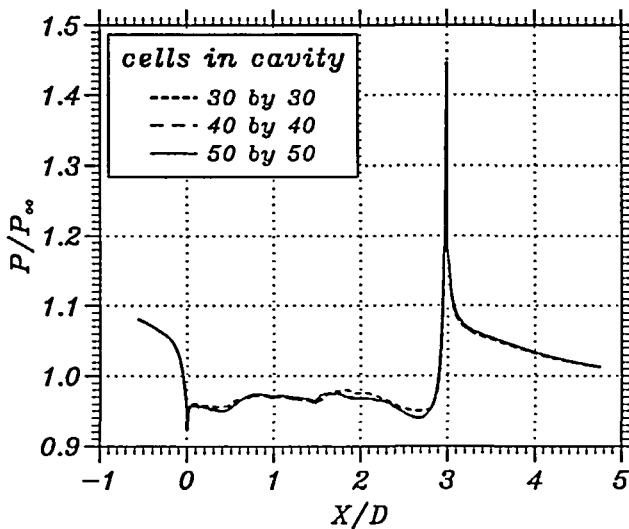*Figure 15* Computed velocity vectors within the cavity

Figure 16 Pressure distribution around cavity surface. The distance X is the wetted distance, commencing at the forward lip

point along the cavity wall and D is the cavity depth. The Stanton number distributions with X/D are given in *Figure 17*. Both these figures show very close agreement between the three solutions, especially between the second and the third mesh. The small differences that can be detected upon closer inspection could suggest the need for further mesh refinement and we will continue working in that direction. However, the difference between the results from the second and the third mesh is so small that in practice a 40 by 40 cell mesh in the cavity provides a sufficiently converged solution. The surface heat transfer rate over most of the cavity is determined
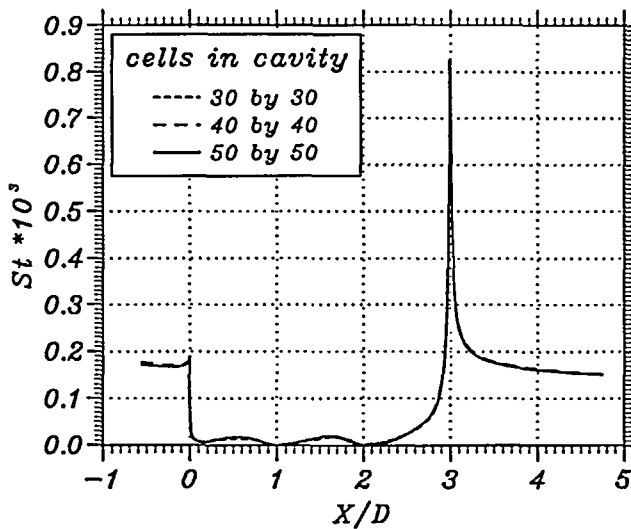
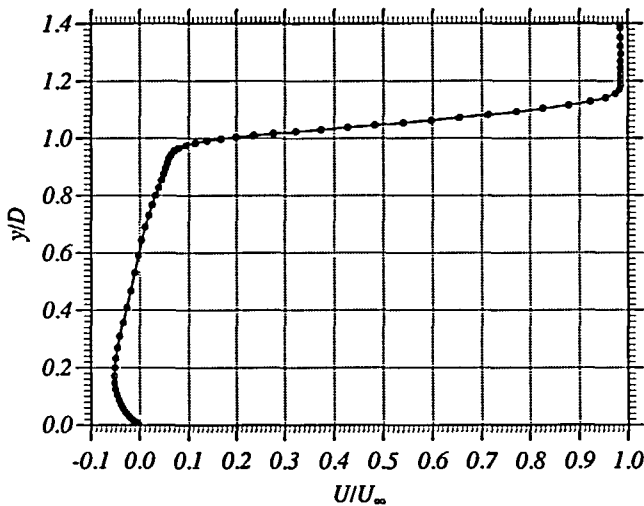*Figure 17*   Stanton number distribution around the cavity

Figure 18   U-velocity profile, in vertical direction commencing at cavity floor, 13.29 mm from front of cavity

to be around 0.1 W/cm² which will require extreme care in measurements. *Figure 18* presents a vertical velociy profile approximately through the centre of the main vortex in the cavity. It can be seen that the free shear layer spread at this Reynolds number is small compared with the cavity depth but is still adequate for profile measurement. The velocity profile parallel to the cavity floor through the vortex centre is given in *Figure 19*.

Experimental work so far has been limited to afterbody heat transfer measurments, and our next phase of experiments will be to study the cavity zone itself. These afterbody measurements
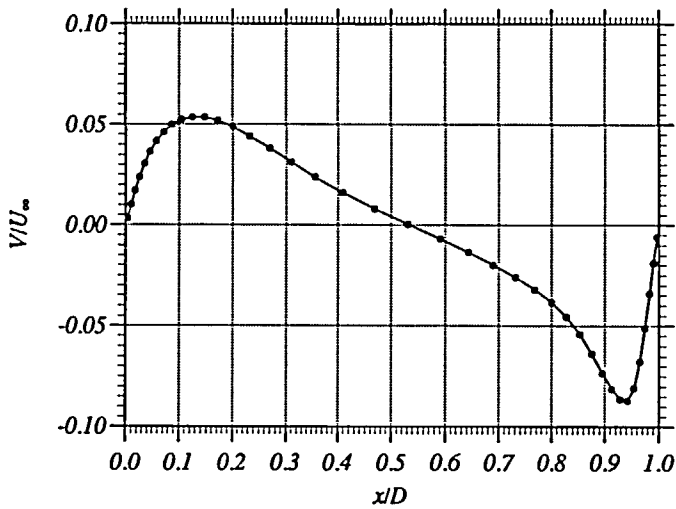
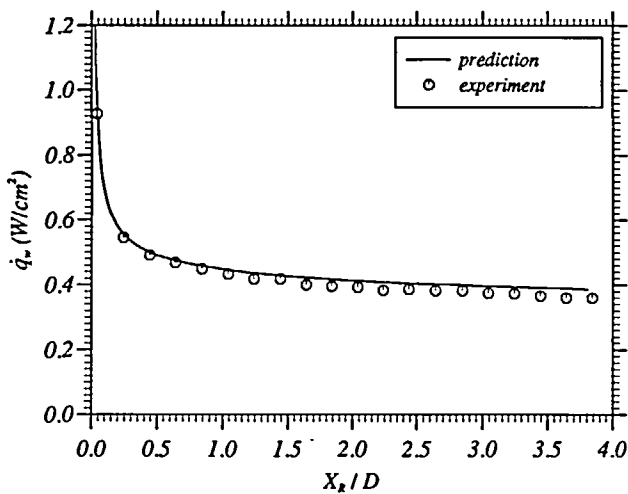*Figure 19* V-velocity profile, in horizontal direction 14.77 mm above cavity floor

Figure 20 Comparison of computed and measured afterbody heat transfer rates for the L/D=1 cavity

were performed primarily to establish whether or not the separated flow is fully laminar. We have established that this is indeed the case, provided tha cavity length to depth ratios L/D are less than six, and a full discussion of the supporting arguments and results can be found in Reference 8. A comparison between the computed and measured afterbody heat transfer rates for the L/D=1 cavity is shown in *Figure 20*. A very good agreement is evident. Although this comparison is perhaps not quite so taxing and definitive as the cavity zone itself, the afterbody still provides a severe test since the boundary layer has anyway had to experience the developments as a separated shear layer over the cavity and the distortions of the reattachment process.
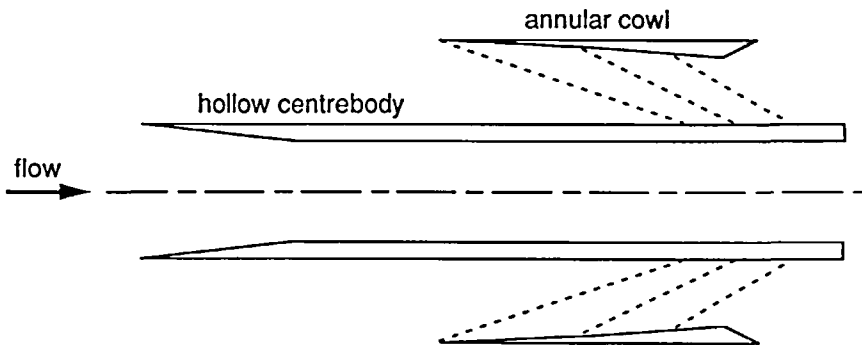
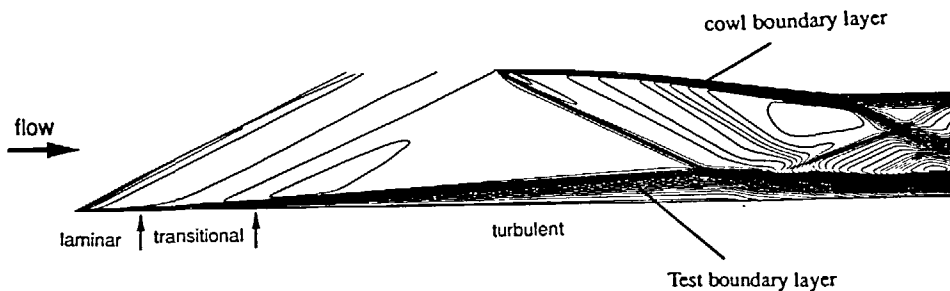*Figure 21* Schematic of hollow cylinder/cowl configuration

Figure 22 Cross plane density contours with radial direction scaled

COMPUTATION OF TURBULENT BOUNDARY LAYERS

For attached flows our laminar boundary layer computations have demonstrated the high resolution of the basic flow solver. ·We are also engaged in the extensive task of assessment of turbulence models and here we comment briefly upon some of our work. Our objective, again a combined CFD/experiment study, is to investigate the behaviour of turbulent boundary layers subjected to adverse pressure gradients. The experimental design logic has followed that outlined in the previous section, and is based upon axisymmetric configurations since this avoids the end effects associated with planar models and ensures the best possible quality of two dimensional flow. We have developed a hollow cylindrical centrebody, which generates the basic 'zero pressure gradient' test boundary layer, which can then be radiated by the pressure field generated by a carefully profiled concentric cowl. A schematic of this arrangement is shown in *Figure 21*. The centrebody is 75 mm in diameter; the cowl inner surface is defined in Appendix 2; it is carefully profiled, with a leading edge diameter of 130 mm and is positioned 340 mm from the leading edge of the centrebody.

The computations now use the simple two layer algebraic eddy viscosity model of Baldwin and Lomax[9] with a 70 mesh criterion enforced for the boundary layer. The experiments are conducted at a nominal Mach number of 8.9 and unit Reynolds number of 52×16^6/metre with a detailed nozzle calibration showing a weak positive axial Mach number gradient along the test flow. This gradient effect is included in the computations. The measured (by surface heat transfer) transition onset and completion on the centrebody, at 80 mm and 170 mm respectively,
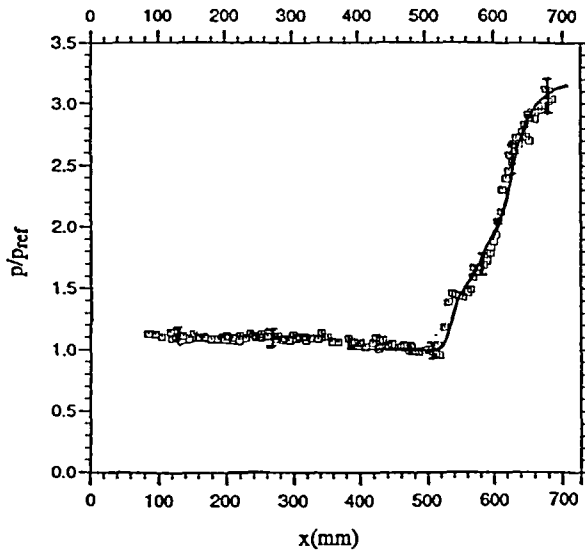
Figure 23 Comparison of measured and computed surface pressures on centrebody. The streamwise scales should be interpreted in conjunction with *Figure 22*
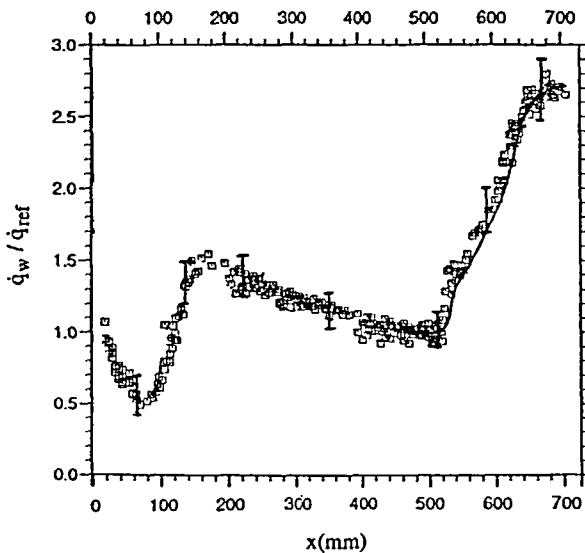

Figure 24 Comparison of measured and computed heat transfers on centrebody

are used to control the progressive switching on of the turbulence model in the computation according to the model of Dhawan and Narasimha[10]. Two predictions are shown. In *Figure 22* the cross plane density contours are given (the radial direction is stretched by a factor of 5 for clarity) and as well as highlighting the test boundary layer it indicates other regions of significance such as the leading edge viscous interactions for the centrebody and cowl. *Figures 23* and *24* compare measured and predicted surface pressures and heat transfer on the centrebody in the

pressure gradient interaction zone. Here the data are normalised by reference values taken at a chord length of 520 mm, that is in the nominally zero pressure gradient flow immediately upstream of the onset of the interaction. These comparisons show good agreement. The onset of the interaction is reproduced very well; not quite the straightforward task it might seem because it is dependent upon the details of the cowl computation and both the cowl and centrebody boundary layers. The total pressure and heat transfer increases are predicted vey well, as is also the detail of the distribution. In particular, even the inflection in the profile at a pressure rise of 1.5:1, which is a consequence of the viscous interaction shock from the cowl, is well duplicated; this is an undesirable side effect, however, and in future designs we would propose to redesign the cowl leading edge to remove this feature and concentrate on generating nearly linear gradients.

CONCLUDING REMARKS

The flow solver combines a high resolution upwind Euler scheme with centred differencing for the diffusive terms. Coupled with a mesh construction routine, which can enforce various criteria for the boundary layer and the external inviscid flow, this has provided high quality attached flow solutions for relatively low mesh densities. The method is currently being extended into modelling of separated flows, in conjunction with a parallel experimental study.

ACKNOWLEDGEMENTS

APPENDIX 1

Formulation of the forebody coordinates

The outer profile of the forebody consists of two straight lines with a curved part in between. Referring to *Figure 8* the coordinates of these three segments, in millimetres, are given by:

- $0 \leqslant x \leqslant 34.7444$; $y = 37.5 + 0.267949x$
- The curved part from $x = 34.7444$ to 172.913 consists of a pair of symmetrical Euler spirals each of 70 mm length where the local coordinates can be obtained from:

$$\begin{cases} xl = s - \dfrac{s^5}{40K^2} + \dfrac{s^9}{3456K^4} \\ yl = \dfrac{s^3}{6K} - \dfrac{s^7}{336K^3} + \dfrac{s^{11}}{42240K^5} \end{cases}$$

where s is the distance along a spiral and $K = 18716.6$. The global coordinates can then be obtained from:

first half $0 \leqslant s \leqslant 70$; $\begin{cases} x = 34.7444 + 0.965926xl + 0.258819yl \\ y = 46.8097 + 0.258819xl - 0.965926yl \end{cases}$

second half $70 \geqslant s \geqslant 0$; $\begin{cases} x = 172.913 - xl \\ y = 65 - yl \end{cases}$

- $172.913 \leqslant x \leqslant 200$; $y = 65$

APPENDIX

Geometry data for the cowl

The cowl inner surface for the turbulent boundary layer study is given by:

$$y = 65 - 7.434 \times 10^{-5}x - 1.086 \times 10^{-4}x^2$$
$$- 3.366 * 10^{-8}x^3 \text{ for } 0 < x < 157.4 \, mm$$

and

$$y = 67.247 - 2.946 \times 10^{-2}x$$
$$- 8.835 \times 10^{-6}x^2 + 9.641 \times 10^{-9}x^3$$
$$\text{for } 157.4 < x < 270 \, mm$$

where $y(mm)$ is the radial distance from the axis of symmetry, $x(mm)$ is the chordwise distance from the cowl leading edge, and the cowl leading edge is positioned at 450 mm from the leading edge of the centrebody.

REFERENCES

1 Ben-Artzi, M. and Falcovitz, J. A high resolution upwind scheme for quasi 1-D flows, *Proc. of the Euler equations workshop*, (eds F. Angrand and R. Glowinski), INRIA, SIAM (1983)
2 Ben-Artzi, M. and Falcovitz, J. A second-order Godunov-type scheme for compressible fluid dynamics, *J. Comp. Phys.*, **55**, 1–32 (1984)
3 Hillier, R. Numerical modelling of shock wave diffraction, *Shock Wave Journal*, **1**, 89–98 (1991)
4 Netterfield, M. P. and Hillier, R. Experiment and computation in hypersonic cavity flows, *AIAA Paper No. 89-1842, AIAA 20th Fluid Dynamics, Plasma Dynamics and Lasers Conf.* (1989)
5 Hillier, R. and Netterfield, M. P. Computation of shock diffraction and unsteady shock wave boundary layer interaction, *Shock Tubes and Waves, AIM*, (ed. Y. W. Kim), 228–233 (1990)
6 Hillier, R., Kirk, D. C., Sell, M. and Soltani, S. Studies of hypersonic viscous flows, *AGARD 70th Fluid Dynamics Panel Meeting and Symp.: Theor. and Exp. Meth. in Hypersonic Flows*, Paper 32 (1992)
7 Van Driest, E. R. Investigation of laminar boundary layer in compressible fluid using the Crocco method, *NACA TN 2597* (1952)
8 Soltani, S. and Hillier, R. An experimental and computational study of hypersonic cavity flows, *AIAA Paper No. 94-0766, 32nd Aerospace Sciences Meeting*, Reno, Nevada (1994)
9 Baldwin, B. S. and Lomax, H. Thin layer approximation and algebraic model for turbulent separated flows, *AIAA Paper No. 78-0257* (1978)
10 Dhawan, S. and Narasimha, R. Some properties of boundary layer flow during the transition from laminar to turbulent motion, *J. Fluid Mech.*, **3**, 4 (1958)